Research Article | Vol. 28, No. 21 / 12 October 2020 / *Optics Express* 32173

Optics EXPRESS

Supercontinuum generation in tantalum pentoxide waveguides for pump wavelengths in the 900 nm to 1500 nm spectral region

JONATHAN R. C. WOODS,[1,*] JAKE DAYKIN,[1] AMY S. K. TONG,[2] COSIMO LACAVA,[2] PERIKLIS PETROPOULOS,[2] ANNE C. TROPPER,[1] PETER HORAK,[2] JAMES S. WILKINSON,[2] AND VASILIS APOSTOLOPOULOS[1]

[1] *School of Physics and Astronomy, University of Southampton, University Road, Southampton, Hampshire, SO17 1BJ, UK*
[2] *Optoelectronics Research Centre, University of Southampton, University Road, Southampton, Hampshire, SO17 1BJ, UK*
[*] *J.Woods@soton.ac.uk*

Abstract: We characterize the spectral broadening performance in silica clad and unclad Tantalum pentoxide (Ta_2O_5) waveguides as a function of the input pulse central wavelength and polarization, sweeping over a wavelength range from 900 nm to 1500 nm, with an average incident power of 110 mW. The waveguides are 0.7 µm high and between 2.2 and 3.2 µm wide, and the SiO_2 top cladding layer is 2 µm thick. We model the dispersion of the higher order spatial modes, and use numerical simulations based on the generalized nonlinear Schrödinger equation to analyze the nonlinear behaviour of the spatial modes within the waveguides as well as the dispersive effects observed in the experiments. We achieve octave spanning supercontinuum with an average power of 175 mW incident on the waveguide at 1000 nm pump wavelength.

1. Introduction

During the last two decades, supercontinuum and frequency comb generation through spectral broadening in waveguide and micro-resonator systems has developed into a rich field of research [1–6]. Planar waveguides offer small guiding areas and large index contrast between core and cladding, leading to high modal confinement, increased effective nonlinear coefficient and reduced bend loss. In the context of nonlinear optics, and in the limit of sufficiently low coupling and propagation losses, tight guiding corresponds to high nonlinear conversion efficiencies. Furthermore, careful design of waveguide geometry can facilitate tailoring of the second order dispersion profiles. When combined, these properties provide a platform where supercontinuum generation may be achieved in only a few millimeters of pulse propagation within the waveguides, and Kerr comb generation may be achieved in exceptionally high repetition rate micro-resonators. Among the various material systems, some waveguide materials may also be fabricated with a CMOS compatible process, enabling low cost, mass producible fabrication in existing facilities.

Materials used in the fabrication of planar waveguides and micro-resonators include Si, SiO_2, Ge, SiON, Si_3N_4, AlN, AlGaAs, and Ta_2O_5 [1,7–10]: of which Tantalum pentoxide (or tantala) has recently observed a spike in interest [11–15]. It is reported that Ta_2O_5 has an optical nonlinearity coefficient n_2 of approximately 3× that of Si_3N_4 [16,17], as well as a thermo-optical coefficient an order of magnitude lower than Si_3N_4 and two orders of magnitude lower than Si [18–20]. Tantala also exhibits a broad transparency window between 300 nm and 8000 nm, a high bandgap energy of 3.8 eV - which facilitates exceptionally low nonlinear 2-photon absorption

#403089 https://doi.org/10.1364/OE.403089
Journal © 2020 Received 20 Jul 2020; revised 9 Sep 2020; accepted 11 Sep 2020; published 9 Oct 2020

- and is also among the materials whose fabrication is CMOS compatible. Until 2017, the lowest reported propagation loss in a Ta_2O_5 waveguide stood at 0.06 dB/cm [12], which utilised waveguide cores fabricated from SiO_2-Ta_2O_5. A record low propagation loss of 0.03 dB/cm was reported in Ref. [14] where, owing to the very thin tantala waveguide layer, a large portion of mode profile propagates in the SiO_2 cladding layer, which would make this geometry exhibit a reduced effective nonlinear coefficient. An often overlooked yet fundamental advantage of tantala as a material for waveguide fabrication is its ability to host rare-earth ions, which enables the fabrication of waveguide optical amplifiers. To date, tantala waveguides have been demonstrated to lase with Er, Yb, and Nd [21–23].

The majority of previous reports of spectral broadening in tantala planar waveguides have explored specific waveguide geometries with a fixed pumping carrier wavelength [15,24–26]. Chaipiboonwong *et al* presented a numerical study of spectral broadening in rectangular Ta_2O_5 waveguides in the visible to NIR region (400 - 950 nm), over multiple spatial modes [25], and the importance of the dispersion of higher order spatial modes when designing waveguides is highlighted. We present an experimental and numerical characterisation of the spectral broadening performance in silica (top) clad as well as unclad Ta_2O_5 waveguides as a function of the input pulse central wavelength and polarisation, sweeping over a wavelength range from 900 nm to 1500 nm. We discuss the experimental results using the calculated dispersion curves of the guided (spatial) modes in the experimentally explored pump central wavelength range, and we present numerical simulations of the generalized nonlinear Schrödinger equation (GNLSE) [27,28] to further understand the waveguide system. Inverse tapers and indeed other engineered waveguide coupling mechanisms have been incorporated into waveguide designs with good success in the literature [29,30]. However, the addition of sub-µm coupling geometries adds further degrees of experimental freedom and therefore complexity. Our intention here is to avoid using waveguides of sub-µm dimensions since they are very sensitive to fabrication errors. We have studied an alternative and simple system of fully etched tantala waveguides between 2.2 and 3.2 µm wide for the entire wavelength range under investigation. With the chosen materials and geometry, single mode operation throughout the pump wavelength range is not possible. An objective intrinsic to this work is to investigate whether we can predict, in this waveguide system, the spectral broadening performance of waveguides that support multiple spatial mode operation. As Ta_2O_5 combines high nonlinearity with the capability of implementing lasers with output wavelengths in the range of 1 to 2.2 µm, there is scope that it can be an appropriate material for integrated supercontinuum generation in an extended wavelength range.

2. Waveguide fabrication and experimental setup

Our fabrication process begins with 4" silicon wafers with a 2.5 µm thick thermal oxide layer on the top (polished) face. On top of this silica layer we deposit the desired thickness of Ta_2O_5 by RF sputtering, and anneal at 600 °C for 2 hours in an oxygen atmosphere for improved stoichiometry and to relieve stress in the film. The sputtering conditions are the same as those used for the fabrication of the low loss erbium-doped Ta_2O_5 slab waveguides presented in [31]. Resist (ZEP-520A) is spin-coated on the wafer before e-beam lithography is used to pattern the waveguides. The wafers are then (fully) etched by ion beam milling to generate the spatial profile of the waveguides, see Fig. 1. At this point, in order to achieve buried (clad) waveguides from the existing ridge (unclad) waveguides, a 2 µm thick layer of SiO_2 is deposited by RF sputtering. The waveguides are isolated from the rest of the wafer by dicing, and the end faces are polished to achieve a good optical coupling interface. We have measured the losses in similar waveguides to those used in our experiments by performing a Fabry-Perot cavity spectral measurement of the light at the output of the waveguide [32] using a narrow linewidth, tunable external cavity diode laser around 1550 nm emitting on a single fundamental spatial mode. Our measurements on a comparable 0.7×2 µm thick, SiO_2 clad waveguide show that the propagation loss is ~

1.4 dB/cm. Furthermore, since the higher order spatial modes that we investigate in this work will usually have greater propagation loss, we expect that the loss measurement represents only a lower limit. During numerical modelling, we use propagation loss values between 3 and 4 dB/cm for the cladded waveguides. We expect that the propagation losses to be increased for unclad waveguides due to the sidewall surface roughness. Indeed comparison between the NLSE model output and the $2.2 \times 0.7\,\mu$m unclad waveguides revealed that the values for the propagation loss were typically higher in order to achieve the closest matches; in the range of 5 - 6.5 dB/cm.

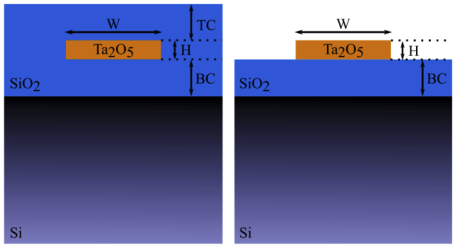

Fig. 1. Tantalum pentoxide waveguide fabrication schematic, depicting the clad and unclad waveguides that we have fabricated by RF sputtering and annealing a tantalum pentoxide layer on top of a thermally oxidised silicon wafer. We have fabricated waveguides that are $0.7\,\mu$m high and between 2.2 and $3.2\,\mu$m wide. BC: bottom cladding, TC: top cladding, Si: Silicon, SiO_2: Silicon Dioxide, Ta_2O_5: Tantalum pentoxide.

The experimental configuration used for this work is given schematically in Fig. 2. In order to investigate the spectral broadening behavior of the waveguides as a function of the pump pulse central wavelength, we use a Coherent Chameleon laser and optical parametric oscillator (OPO) as a highly tunable source of mode-locked laser pulses. The Chameleon system is capable of generating 150 fs pulses at 80 MHz repetition rate with a Ti:Sapphire laser oscillator, where the pulse central wavelength is tunable from 750 nm to 1050 nm. The long wavelength region may be extended into the near IR with the use of the OPO, which gives us access to the wavelength range between 1050 nm and ~1500 nm. While the OPO system provides mode-locked pulses in this extended frequency range, a side effect is marginal broadening of the pulse temporal profile to $\lesssim$ 200 fs. Throughout this work, we use the term *pump wavelength*, which refers to the central (carrier) wavelength of the mode-locked pulses that are coupled to the tantala waveguides.

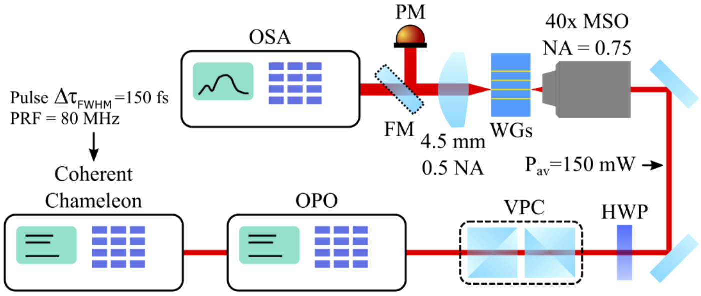

Fig. 2. Experimental apparatus showing how the laser pump was coupled into our waveguide system and the coupling to the optical spectrum analyser.

The bypass and signal outputs from the OPO are aligned coaxially before entering a variable power controller (VPC) used to attenuate the average beam power down to 150 mW. Once attenuated, a half waveplate (HWP) is used to select the TE and TM polarisations before the beam is directed through a 40X microscope objective (NA = 0.75) for coupling to the waveguide.

At the output of the waveguides, a single 4.5 mm focal length aspherical lens (NA = 0.55) is used to collect and collimate the emitted light which, subsequently, is coupled to a multimode fiber and input into the Optical Spectrum Analyser (OSA). It should be noted that 150 mW is the measured power before the microscope objective. The transmission through this objective reduces the incident power on the entrance facet of the waveguide to approximately 110 mW.

3. Spectral broadening performance

We have compared the spectral broadening performance of silica clad and unclad tantala waveguides using a mode-locked laser pump source over a range of central wavelengths from 900 to 1500 nm, using the system shown in Fig. 2. When designing a waveguide geometry there is a range of desirable characteristics, such as high mode overlap with the nonlinear region, low propagation loss, efficient power coupling, single mode operation and high refractive index contrast. It is quite challenging to satisfy all these attributes especially when a wide wavelength range is investigated as it is here. We have generally investigated waveguides between 2.2 and 3.2 μm wide and ~ 18 mm in length.

Our initial result in Fig. 3 was taken using a 2.6 μm × 0.7 μm, SiO_2 clad waveguide, where we achieved an octave spanning emission at around the noise level using an average power of 175 mW incident on the waveguide. The input beam was orientated in the TM polarisation and the pump wavelength was 1000 nm. The results are shown in Fig. 3, where a comparison is made between the collected emission spectrum of the waveguide and the shape of the input pulse spectrum.

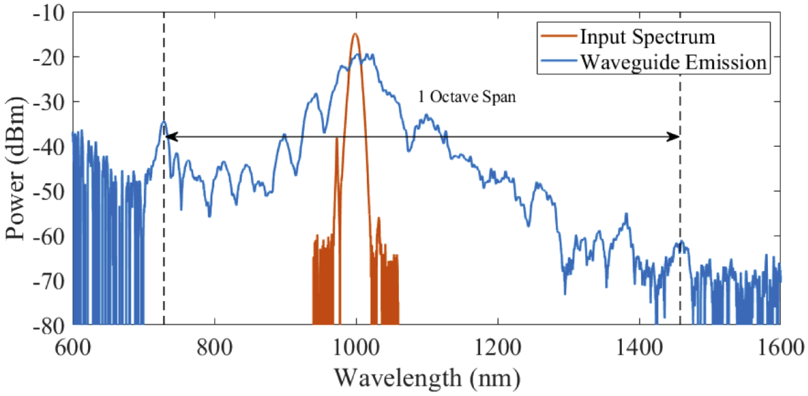

Fig. 3. Demonstration of an octave spanning supercontinuum spectrum emitted from a 2.6 μm × 0.7 μm, SiO_2 clad waveguide. Approximately 175 mW of average power was incident on the input waveguide facet in the TM polarisation.

In Figs. 4 and 5, the spectral broadening performance as a function of the pump wavelength is shown for the 3.2 × 0.7 μm, SiO_2 clad waveguide and the 2.2 × 0.7 μm, unclad waveguide. In each case, the sub-figures (a) and (b) correspond to the input polarisation aligned in the TM and TE orientations (normal and parallel to the waveguide substrate plane) respectively. In both waveguide geometries, it is clear that spectral broadening is increased by the shorter pump wavelength for the TM whereas the TE polarisation conversely shows increased spectral broadening for longer pump wavelengths.

The average power of 175 mW at the waveguide entrance face was not achievable throughout the whole pump wavelength range however, and since the objective of this work is to characterise the dependence on pump wavelength, a reduced pump average power was opted for. The results presented in Figs. 4 and 5 use 110 mW of incident average power in order to maximise the range

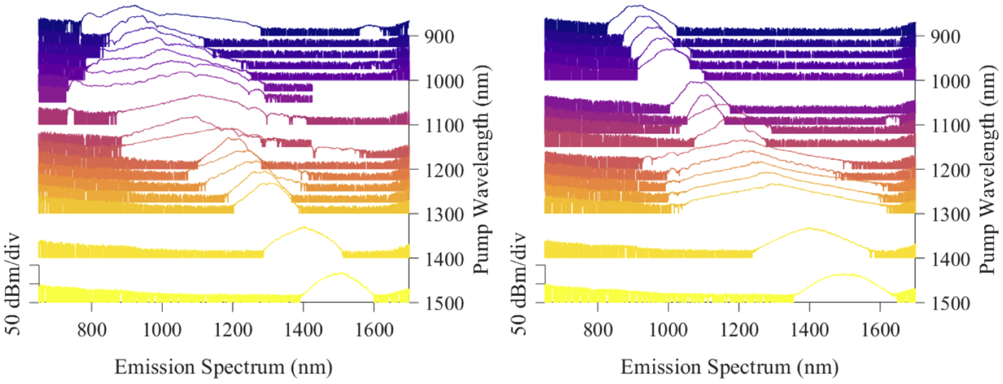

(a) TM Polarisation

(b) TE Polarisation

Fig. 4. Optical spectra collected for a 3.2 μm wide, SiO_2 clad waveguide in the (a) TM and (b) TE polarisations, and with 110 mW of average pulse power at the input facet to the waveguide.

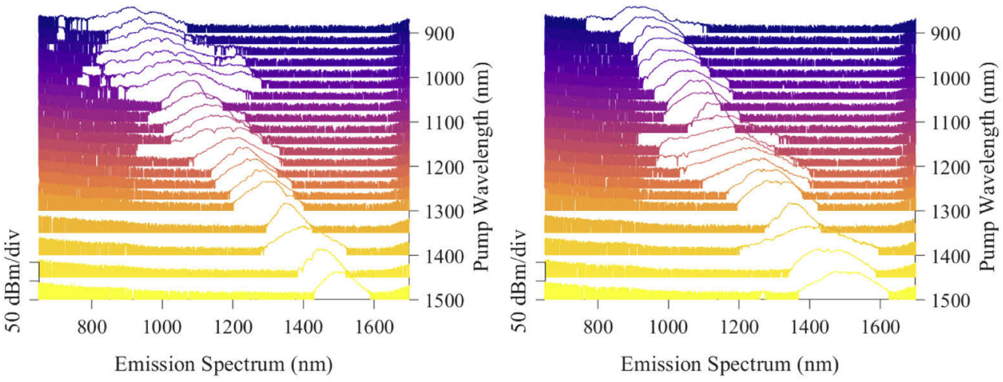

(a) TM Polarisation

(b) TE Polarisation

Fig. 5. Optical spectra collected for a 2.2 µm wide, unclad waveguide in the TM and TE polarisations, and with 110 mW of average pulse power at the input facet to the waveguide.

over which a constant pump power can be generated, and to avoid damaging the waveguide end-facets.

Regarding the insertion losses, we measure the power incident on the front facet of the waveguide in each case (110 mW), and measure the total collected power after the waveguide. For the 3.2 × 0.7 µm, SiO_2 clad guide, the mean value for the collected power at the waveguide output across the pump wavelength range is 1.2 ± 0.07 mW for the TM polarisation, and 1.1± 0.07 mW for the TE polarisation. Similarly, the mean collected powers for the 2.2 × 0.7 µm unclad waveguide output are 0.3 ± 0.02 mW for the TM polarisation, and 0.5 ± 0.05 mW for the TE polarisation. The above power values for the 3.2 × 0.7 µm, SiO_2 clad waveguide correspond to insertion losses of 19.6 dB for the TM polarisation, and 20.0 dB for the TE polarisation. Similarly, insertion losses for the 2.2 × 0.7 µm, unclad waveguide correspond to 25.6 dB for the TM polarisation, and 23.4 dB for the TE polarisation. It is expected that the unclad guide will have a higher coupling loss due to its asymmetric mode profile and a higher propagation loss because of the higher refractive index contrast and possibly higher roughness. For a given waveguide geometry, both the spatial mode order and wavelength will affect both coupling and propagation losses. We anticipate our losses will be increased by the ion beam milling which gives rise to non-negligible roughness to the waveguide side walls, thereby contributing to the propagation (scattering) loss. In light of this, investigation into reactive gas assisted ion beam milling is in progress. In this study to deconvolve and experimentally quantify the two main sources of loss, namely the coupling and propagation losses we would need to measure the loss as a function of wavelength and as a function of waveguide mode. This is a very difficult task and consequently we use the waveguide coupled power (coupling loss) and propagation loss as free parameters in the nonlinear numerical modelling presented in section 4.

4. Dispersion and nonlinear Schrödinger equation simulations

In order to interpret the results we have used the commercial software package Lumerical to simulate our waveguides and obtain group velocity dispersion curves. Due to the high refractive index of the tantala waveguide layer, the waveguides exhibit multimode behavior throughout our pump wavelength range. Figure 6(a) shows the simulated dispersion parameter, D (ps / nm / km), for the 3.2×0.7 µm, SiO_2 clad waveguide geometry. The zero-dispersion wavelength (ZDW) for the TM fundamental mode is approximately 1150 nm, whereas the TE fundamental mode does not exhibit anomalous dispersion in this pump wavelength range. It can also be seen that all the TM polarisation spatial modes exhibit ZDWs that are significantly blue shifted when compared with the equivalent spatial mode order for the TE polarisation modes. Furthermore, in Fig. 6 from the higher order modes in both the TE and TM polarisations, it can be seen that the ZDW blue-shifts significantly.

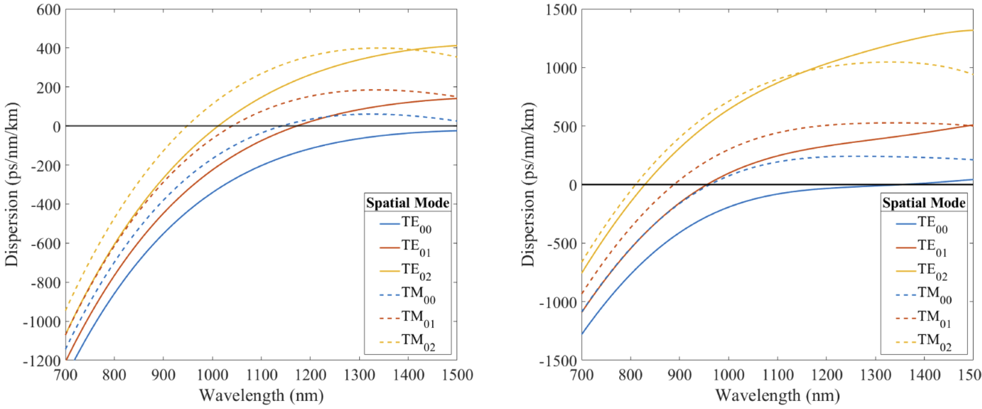

(a) (b)

Fig. 6. Modelled second order dispersion against wavelength for different spatial modes and polarizations. (a) 3.2 µm wide, SiO_2 clad waveguide, and (b) 2.2 µm wide, unclad waveguide.

Figure 6(b) shows similar results for the dispersion for each spatial mode of the 2.2×0.7 µm unclad waveguide. In this case, the fundamental TE spatial mode does become anomalous, and crosses zero dispersion at approximately 1350 nm. The dispersion curves show a similar trend to that of the clad waveguides shown in Fig. 6(a) but shifted towards shorter wavelengths. For instance, the fundamental TM mode dispersion becomes anomalous at the significantly shorter wavelength of 950 nm.

In order to achieve the most efficient spectral broadening in the waveguide, it is generally accepted that the pump wavelength should be in the weakly anomalous dispersion regime. For a target pump wavelength of 1 µm it is clear that, for the TM polarisation fundamental spatial mode inside the waveguide, the unclad waveguide is best suited to supercontinuum generation.

However, from a perspective of propagation loss minimisation, an overcladding layer on the waveguide is desirable in order to decrease losses due to surface roughness. The overcladding also improves the symmetry and increases the size of the waveguide modes which potentially decreases coupling loss.

We compare our experimentally observed supercontinuum spectra with numerical simulations of the generalised nonlinear Schrödinger equation (GNLSE) using a split-step Fourier method with automatic step-size control [27,28]. The simulations assume the optical nonlinearity of Ta_2O_5 to be independent of wavelength and spatial mode, and has the value $n_2 = 7.23 \times 10^{-19}$ m^2/W [16]. Specifically in Fig. 7 we used a wavelength-independent propagation loss of 2 dB/cm, an estimated power launched in the waveguides of 7.5 mW (which assumes a coupling loss of ~12 dB), and the dispersion curves as presented above. Our simulation of the pulse spectral evolution as a function of propagation distance in a 3.2×0.7 µm, SiO_2 clad waveguide is shown in Fig. 7 for the three lowest order (TM polarisation) spatial modes at pump wavelengths of 1000 and 1500 nm.

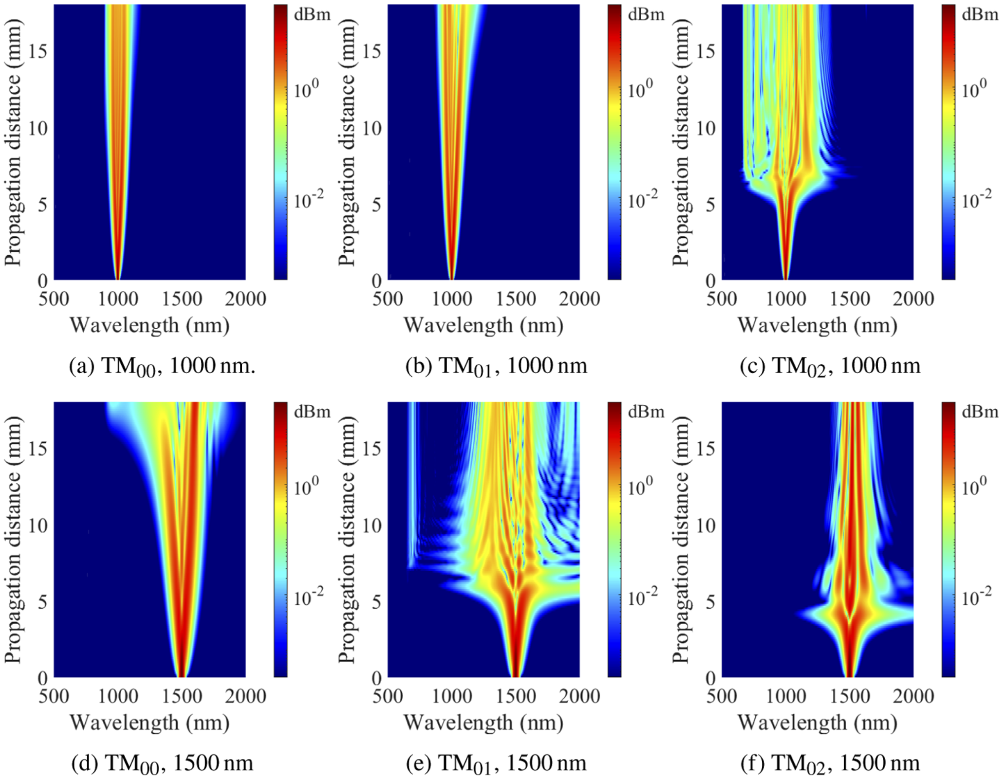

(a) TM_{00}, 1000 nm. (b) TM_{01}, 1000 nm (c) TM_{02}, 1000 nm

(d) TM_{00}, 1500 nm (e) TM_{01}, 1500 nm (f) TM_{02}, 1500 nm

Fig. 7. Simulations of the nonlinear Schrödinger equation for a launched power of 7.5 mW and propagation loss of 2 dB/cm for the first three TM modes in the 1000 and 1500 nm central pump wavelengths for the 3.2×0.7 µm SiO_2 clad waveguide.

Figure 7 shows that significant broadening in the region of 1000 nm is achieved by the TM_{02} mode whereas at 1500 nm broadening can be achieved by the TM_{00} and TM_{01} modes. Therefore, based on our simulations of the dispersion curves, as well as from the solution of the GNLSE, significant spectral broadening at short wavelengths is mostly attributed to higher order modes and at long wavelengths low order modes provide better spectral broadening performance.

Plots depicting the power spectrum of the optical pulse as a surface, such as those in Fig. 7, show the spectral evolution as a function of distance. However, as we are unable to observe experimentally the optical spectrum at positions within the waveguide, we compare measured optical spectra with simulated spectra at the output of the waveguide. In Figs. 8 and 9 we show comparisons of experimentally and numerically obtained spectra for the 3.2×0.7 µm, SiO_2 clad

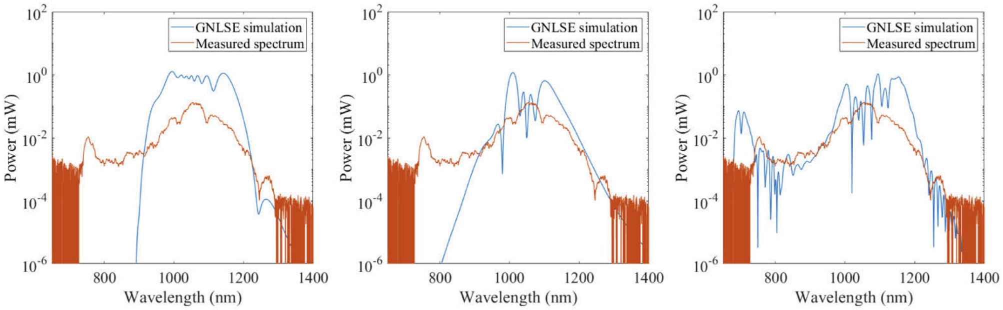

(a) TM_{00}, 3.00 dB/cm, 12.1 mW (b) TM_{01}, 3.00 dB/cm, 4.4 mW (c) TM_{02}, 3.25 dB/cm, 5.8 mW

Fig. 8. Comparison of experimental data for spectral broadening in a 3.2×0.7 µm SiO_2 clad waveguide at a pump wavelength of 1050 nm and the GNLSE-based simulation of the three lowest order propagating spatial modes at 1050 nm. The model free parameters and the specific values used for each simulation are given in the caption for each subfigure.

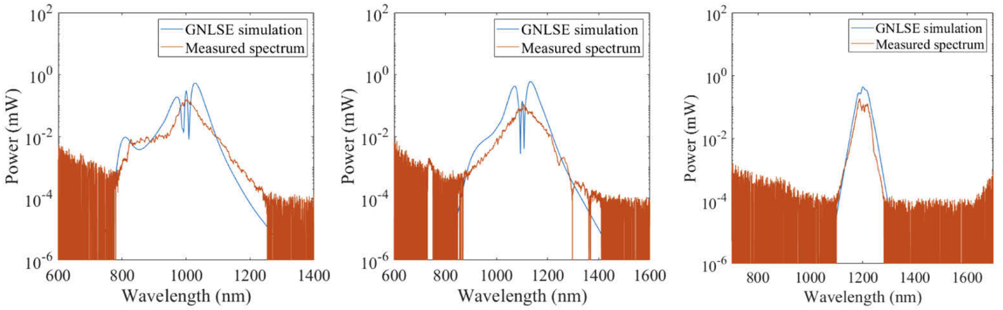

(a) 1.0 µm TM_{02} 3 dB/cm 2.0 mW (b) 1.1 µm TM_{01} 3 dB/cm 2.6 mW (c) 1.2 µm TM_{01} 4 dB/cm 1.5 mW

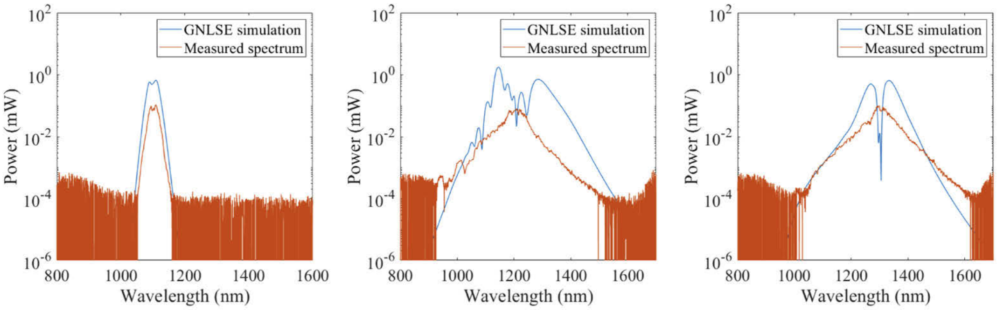

(d) 1.1 µm TE_{01} 3 dB/cm 1.5 mW (e) 1.2 µm TE_{01} 3 dB/cm 6.1 mW (f) 1.3 µm TE_{01} 3 dB/cm 2.4 mW

Fig. 9. Comparison of experimental data for spectral broadening in a 3.2×0.7 µm SiO_2 clad waveguide at multiple pump wavelengths and over both polarisation states, and the GNLSE-based simulation of the same experimental parameters. In each case the three free parameters for the simulations are shown on each sub-figure. In the cases of sub-figures 9(a), 9(e), 9(f), it is likely that , it is likely that the experimental spectra are comprised of optical power that is coupled into more than one waveguide spatial mode.

waveguide at various pump wavelengths for both polarisation states. In these plots the final calculated pulse spectrum from the GNLSE model is compared directly to the OSA trace, where the dispersion curves from Fig. 6(a) are used intrinsically in the GNLSE model. We have assumed that the experimental losses between the waveguide end facet and the input to the fiber coupled OSA are negligible. In Figs. 8 and 9 the variable parameters used in generating simulations to match the experimental spectra acquired are the spatial mode order, propagation loss (between 3 dB/cm and 4 dB/cm) and coupled optical power. Specifically in Fig. 9, comparison is made between experimental data and only the best matching simulated spatial mode in each case, i.e. the modelled spectrum is chosen based on how well each spatial mode represents the overall shape of the data.

In Fig. 8 we show a comparison of the modelled and experimental spectral data at 1050 nm pump wavelength propagating in the $3.2 \times 0.7\,\mu\text{m}$, SiO_2 clad waveguide. In this figure, sub-figures (a) - (c) represent the $TM_{00,01,02}$ modes respectively. Clearly the TM_{02} spatial mode best represents the overall shape of the recorded optical spectrum in terms of the coarse shape, and exhibits coupling to the dispersive wave at the blue end of the spectrum.

Figure 9 shows the comparison between the recorded data over a 200 nm region from 1000 - 1200 nm for the TM polarisation and 1100 - 1300 nm for the TE polarisation, and the best matching model results for the same range. With reference to Figs. 4(a) and 4(b), we chose the ranges around the pump wavelength at which the TM (TE) polarisation state exhibits a deterioration (improvement) of the spectral broadening performance with increasing pump wavelength.

5. Discussion

In the case of the clad waveguides, the TM polarisation experimental results are shown in Fig. 4(a). At the shortest pump wavelength of 900 nm, the predominant mechanism for spectral broadening is that of high order soliton fission, with phase matching to the dispersive wave across the ZDW giving rise to the peak in the emission spectrum at around 800 nm [27]. The total spectral width of the supercontinuum generation here is approximately 500 nm, having broadened asymmetrically around the 900 nm pump wavelength. The presence of the dispersive wave at the blue end of the spectrum in Fig. 4(a) implies that the 900 nm pump wavelength resides in the anomalous region of the modal dispersion within the waveguide. From Figs. 6(a) and 6(b) we can see that the ZDWs are significantly blue shifted for higher order modes. Therefore, taking into account the dispersion curves shown in Fig. 6, it is expected that the majority of the optical power is coupled to a spatial mode other than the fundamental. This is also supported in Figs. 7(a), 7(b), and 7(c) where it is shown that only higher order modes achieve significant spectral broadening at shorter wavelengths. Figures 8(a), 8(b), and 8(c) demonstrate the comparison of the data recorded for the pump wavelength of 1050 nm with the three simulated lowest order spatial modes. It is clear from the figures that the TM_{02} best represents the majority of the salient spectral features. In Fig. 4(a) at pump wavelengths between 1100 nm and 1175 nm, it is likely that the optical power coupling to lower order modes starts to dominate. Furthermore, this is also supported in Fig. 9 where, in sub-Figs. 9(a), 9(b), and 9(c), there is a transition from 1000 to 1200 nm from the TM_{02} to TM_{01}. It is also very likely that for the 1.1 µm pump wavelength the emission spectrum consists of a superposition of coupled spatial modes. For pump wavelengths longer than 1250 nm and up to 1500 nm, the spectral behavior typically exhibits a relatively narrow degree of spectral broadening, around 200 - 300 nm at the noise level, and the rounded, smoother spectral shape is indicative of low order soliton propagation. Behaviour of this nature is typically associated with pumping within the anomalous region of the spectral dispersion. Comparison of the experimental results with the simulations of Figs. 7(d), 7(e), and 7(f) supports our interpretation that at 1500 nm pump wavelength the spectrum is mainly generated in the fundamental TM mode since the TM_{01} mode would provide much wider broadening and at 1500 nm wavelength we are unlikely to couple into the TM_{02} mode.

Considering now the TE polarisation for the 3.2×0.7 µm, SiO_2 clad waveguide which is shown in Fig. 4(b), we observe spectral behavior that is consistent with optical coupling into a higher order spatial mode in the range from 900 - 1300 nm. Between pump wavelengths of 900 - 1100 nm, the spectra exhibit behavior consistent with broadening via self phase modulation. As the pump wavelength increases towards 1200 - 1300 nm, the spectral width increases dramatically as we approach, and likely cross, the zero dispersion wavelength of the TE_{01} mode, as shown in Fig. 6(a). In Figs. 9(a), 9(e), and 9(f) we see that the TE_{01} can approximate the data throughout the wavelength range. Due to the complexity of the simulated system, it is not possible to try to match the experiment perfectly. Beyond this region, when pumping towards 1400 - 1500 nm, the spectral broadening performance drops and the spectrum smooths. Similarly to the TM polarisation, it is believed that we are coupling into the fundamental TE mode.

In general, it was found that the unclad waveguides were less efficient in generating supercontinuum, for both input polarisation states, as can be seen in Fig. 5(a) and 5(b). This is not due to the dispersion of the unclad waveguides (Fig. 6(b)), but rather likely because of a higher coupling loss owing to the smaller spatial mode volume, and a higher propagation loss caused by the tantala layer top surface roughness. The spectral broadening performance of the 2.2×0.7 µm unclad waveguide exhibits a similar pattern of behavior, despite the noticeable drop in the degree of absolute spectral broadening. In Fig. 5(a), shorter wavelengths show significantly better spectral broadening performance. Furthermore, at the pump wavelength of 925 nm, the same brief narrowing behavior is observed as in Fig. 4(a), before broadening again to approximately 500 nm at the noise level. Similarly the TE polarisation in Fig. 5(b) exhibits better performance for wavelengths above 1200 nm: behavior that is comparable to the clad waveguide shown in Fig. 4. At pump wavelengths greater than 1050 nm, the spectral broadening drops to approximately 200 - 300 nm at the noise level, and it is expected that again we are coupling in the anomalous dispersion regime. The unclad waveguides had the advantage that their ZDW was blue shifted in relation to the clad waveguides; however, we believe that the high losses resulted in reduced overall spectral broadening for the same incident power.

Our analysis has shown that the combination of waveguide simulation (the commercial program Lumerical, in our case) and NLSE provide results of sufficient accuracy for the reliable design of tantala waveguides that can be used to generate nonlinear spectral broadening over a wide wavelength range. Furthermore, through the appropriate use of polarisation and propagating spatial mode order, our results show that it is possible to generate broadband supercontinuum in a single, above sub-micron dimension waveguide, for pump wavelengths ranging from at least 900 nm to 1400 nm.

6. Conclusion

We have presented a study of the spectral broadening behavior in both SiO_2 clad and unclad tantalum pentoxide waveguides, as a function of pump wavelength and pump polarisation state, and have shown that broadband supercontinuum can be generated with only $\leq$10 mW of coupled average power. Owing to the dimensions of the core region of the guides under test, single fundamental spatial mode propagation is not possible over the entire pump wavelength range. Nevertheless, despite the waveguide core dimensions, our modelling and experimental results shows not only a very good agreement for the spectral broadening behavior of higher order spatial mode propagation, but also that our fabricated waveguides match, with sufficient accuracy, to the calculated dispersion curves. Furthermore we have demonstrated that, owing to propagation in a higher order spatial mode, the anomalous dispersion region can be reached with SiO_2 clad waveguides, and in a future design we believe that a continuous octave spanning spectrum performance can be achieved over the range of 900 - 1500 nm. For similar waveguide dimensions presented in this work, partially etched profiles will enable us to approach single mode operation and adequate coupling efficiency.

All data supporting this study are openly available from the University of Southampton repository at: https://doi.org/10.5258/SOTON/D1529

Funding

Engineering and Physical Sciences Research Council (EP/L00044X/1, EP/M013294/1, EP/T001046/1).

Disclosures

The authors declare no conflicts of interest.

References

1. A. Pasquazi, M. Peccianti, L. Razzari, D. J. Moss, S. Coen, M. Erkintalo, Y. K. Chembo, T. Hansson, S. Wabnitz, P. Del'Haye, X. Xue, A. M. Weiner, and R. Morandotti, "Micro-combs: A novel generation of optical sources," Phys. Rep. **729**, 1–81 (2018).
2. T. Herr, V. Brasch, J. D. Jost, C. Y. Wang, N. M. Kondratiev, M. L. Gorodetsky, and T. J. Kippenberg, "Temporal solitons in optical microresonators," Nat. Photonics **8**(2), 145–152 (2014).
3. T. Herr, K. Hartinger, J. Riemensberger, C. Y. Wang, E. Gavartin, R. Holzwarth, M. L. Gorodetsky, and T. J. Kippenberg, "Universal formation dynamics and noise of Kerr-frequency combs in microresonators," Nat. Photonics **6**(7), 480–487 (2012).
4. L. Razzari, D. Duchesne, M. Ferrera, R. Morandotti, S. Chu, B. E. Little, and D. J. Moss, "CMOS-compatible integrated optical hyper-parametric oscillator," Nat. Photonics **4**(1), 41–45 (2010).
5. J. S. Levy, A. Gondarenko, M. A. Foster, A. C. Turner-Foster, A. L. Gaeta, and M. Lipson, "CMOS-compatible multiple-wavelength oscillator for on-chip optical interconnects," Nat. Photonics **4**(1), 37–40 (2010).
6. F. Ferdous, H. Miao, D. E. Leaird, K. Srinivasan, J. Wang, L. Chen, L. T. Varghese, and A. M. Weiner, "Spectral line-by-line pulse shaping of on-chip microresonator frequency combs," Nat. Photonics **5**(12), 770–776 (2011).
7. D. J. Moss, R. Morandotti, A. L. Gaeta, and M. Lipson, "New CMOS-compatible platforms based on silicon nitride and Hydex for nonlinear optics," Nat. Photonics **7**(8), 597–607 (2013).
8. Y. Okawachi, K. Saha, J. S. Levy, Y. H. Wen, M. Lipson, and A. L. Gaeta, "Octave-spanning frequency comb generation in a silicon nitride chip," Opt. Lett. **36**(17), 3398–3400 (2011).
9. A. C. Turner, M. A. Foster, A. L. Gaeta, and M. Lipson, "Ultra-low power parametric frequency conversion in a silicon microring resonator," Opt. Express **16**(7), 4881–4887 (2008).
10. L. Chang, W. Xie, H. Shu, Q.-F. Yang, B. Shen, A. Boes, J. D. Peters, W. Jin, C. Xiang, S. Liu, G. Moille, S.-P. Yu, X. Wang, K. Srinivasan, S. B. Papp, K. Vahala, and J. E. Bowers, "Ultra-efficient frequency comb generation in AlGaAs-on-insulator microresonators," Nat. Commun. **11**(1), 1331 (2020).
11. P. Rabiei, A. Rao, J. Chiles, J. Ma, and S. Fathpour, "Low-loss and high index-contrast tantalum pentoxide microring resonators and grating couplers on silicon substrates," Opt. Lett. **39**(18), 5379 (2014).
12. M. Itoh, T. Kominato, M. Abe, M. Itoh, and T. Hashimoto, "Low-Loss Silica-Based SiO_2-Ta_2O_5 Waveguides With Extremely High Δ Fabricated Using Sputtered Thin Films," J. Lightwave Technol. **33**(2), 318–323 (2015).
13. C. Lacava, A. Aghajani, P. Hua, D. Richardson, P. Petropoulos, and J. S. Wilkinson, "Nonlinear optical properties of ytterbium-doped tantalum pentoxide rib waveguides on silicon at telecom wavelengths," in *Optical Fiber Communication Conference*, (Optical Society of America, 2016), p. W4E.4.
14. M. Belt, M. L. Davenport, J. E. Bowers, and D. J. Blumenthal, "Ultra-low-loss Ta_2O_5-core/SiO_2-clad planar waveguides on Si substrates," Optica **4**(5), 532 (2017).
15. C. Wu, X. Ding, Z. Wu, and S. Feng, "High repetition rate flat coherent optical frequency comb generation based on the normal dispersion tantalum pentoxide optical waveguide," OSA Continuum **2**(9), 2704 (2019).
16. C.-Y. Tai, J. S. Wilkinson, N. M. B. Perney, M. C. Netti, F. Cattaneo, C. E. Finlayson, and J. J. Baumberg, "Determination of nonlinear refractive index in a Ta_2O_5 rib waveguide using self-phase modulation," Opt. Express **12**(21), 5110 (2004).
17. R. Y. Chen, M. D. B. Charlton, and P. G. Lagoudakis, "Chi 3 dispersion in planar tantalum pentoxide waveguides in the telecommunications window," Opt. Lett. **34**(7), 1135–1137 (2009).
18. A. K. Chu, H. C. Lin, and W. H. Cheng, "Temperature dependence of refractive index of Ta_2O_5 Dielectric Films," J. Electron. Mater. **26**(8), 889–892 (1997).
19. A. Arbabi and L. L. Goddard, "Measurements of the refractive indices and thermo-optic coefficients of Si_3N_4 and SiOx using microring resonances," Opt. Lett. **38**(19), 3878–3881 (2013).
20. J. Komma, C. Schwarz, G. Hofmann, D. Heinert, and R. Nawrodt, "Thermo-optic coefficient of silicon at 1550 nm and cryogenic temperatures," Appl. Phys. Lett. **101**(4), 041905 (2012).
21. B. Unal, M. Netti, M. Hassan, P. Ayliffe, M. Charlton, F. Lahoz, N. Perney, D. Shepherd, C.-Y. Tai, J. Wilkinson, and G. Parker, "Neodymium-doped tantalum pentoxide waveguide lasers," IEEE J. Quantum Electron. **41**(12), 1565–1573 (2005).

22. A. Aghajani, G. S. Murugan, N. P. Sessions, V. Apostolopoulos, and J. S. Wilkinson, "Waveguide lasers in ytterbium-doped tantalum pentoxide on silicon," Opt. Lett. **40**(11), 2549 (2015).
23. A. Aghajani, G. S. Murugan, N. P. Sessions, S. J. Pearce, V. Apostolopoulos, and J. S. Wilkinson, "Spectroscopy of ytterbium-doped tantalum pentoxide rib waveguides on silicon," Opt. Mater. Express **4**(8), 1505 (2014).
24. Y.-Y. Lin, C.-L. Wu, W.-C. Chi, Y.-J. Chiu, Y.-J. Hung, A.-K. Chu, and C.-K. Lee, "Self-phase modulation in highly confined submicron Ta_2O_5 channel waveguides," Opt. Express **24**(19), 21633–21641 (2016).
25. T. Chaipiboonwong, P. Horak, J. D. Mills, and W. S. Brocklesby, "Numerical study of nonlinear interactions in a multimode waveguide," Opt. Express **15**(14), 9040–9047 (2007).
26. R. Fan, C.-L. Wu, Y.-Y. Lin, C.-Y. Liu, P.-S. Hwang, C.-W. Liu, J. Qiao, M.-H. Shih, Y.-J. Hung, Y.-J. Chiu, A.-K. Chu, and C.-K. Lee, "Visible to near-infrared octave spanning supercontinuum generation in tantalum pentoxide (Ta_2O_5) air-cladding waveguide," Opt. Lett. **44**(6), 1512 (2019).
27. J. M. Dudley, G. Genty, and S. Coen, "Supercontinuum generation in photonic crystal fiber," Rev. Mod. Phys. **78**(4), 1135–1184 (2006).
28. F. Poletti and P. Horak, "Description of ultrashort pulse propagation in multimode optical fibers," J. Opt. Soc. Am. B **25**(10), 1645–1654 (2008).
29. J. Liu, A. S. Raja, M. H. P. Pfeiffer, C. Herkommer, H. Guo, M. Zervas, M. Geiselmann, and T. J. Kippenberg, "Double inverse nanotapers for efficient light coupling to integrated photonic devices," Opt. Lett. **43**(14), 3200–3203 (2018).
30. G. Moille, Q. Li, T. C. Briles, S.-P. Yu, T. Drake, X. Lu, A. Rao, D. Westly, S. B. Papp, and K. Srinivasan, "Broadband resonator-waveguide coupling for efficient extraction of octave-spanning microcombs," Opt. Lett. **44**(19), 4737–4740 (2019).
31. A. Z. Subramanian, C. J. Oton, J. S. Wilkinson, and R. Greef, "Waveguiding and photoluminescence in Er^{3+}-doped Ta_2O_5 planar waveguides," J. Lumin. **129**(8), 812–816 (2009).
32. T. Feuchter and C. Thirstrup, "High precision planar waveguide propagation loss measurement technique using a fabry-perot cavity," IEEE Photonics Technol. Lett. **6**(10), 1244–1247 (1994).